Biosensors and Bioelectronics 198 (2022) 113817

Contents lists available at ScienceDirect

Biosensors and Bioelectronics

journal homepage: www.elsevier.com/locate/bios

Target-modulated competitive binding and exonuclease I-powered strategy for the simultaneous and rapid detection of biological targets

Yingwen Wang [a,b,c], Dun Zhang [a,b,c,*], Yan Zeng [a,c], Peng Qi [a,b,c,**]

[a] Key Laboratory of Marine Environmental Corrosion and Bio-fouling, Institute of Oceanology, Chinese Academy of Sciences, Qingdao, 266071, China
[b] University of the Chinese Academy of Sciences, Beijing, 100039, China
[c] Open Studio for Marine Corrosion and Protection, Pilot National Laboratory for Marine Science and Technology (Qingdao), 1 Wenhai Road, Qingdao, 266237, China

ARTICLE INFO

Keywords:
Simultaneous multiple-target detection
UiO-67
Exonuclease I-Powered signal molecule release
ATP
cyt *c*

ABSTRACT

Simultaneous multiple-target detection is essential for the prevention, identification, and treatment of numerous diseases. In this study, a novel strategy based on target-modulated competitive binding and exonuclease I (Exo I)-powered signal molecule release was established with the advantages of rapid response and high selectivity and sensitivity. The strategy holds substantial potential for the development of versatile platforms for the simultaneous detection of biological targets. To mitigate the low load capacity and time-consuming responsive process of the Zr-MOF system, UiO-67 was chosen to replace UiO-66 (a typical Zr-MOF) as the nanocarrier for encapsulating more signal molecules, whereby the assembled double-stranded DNA (dsDNA) structures of UiO-67 acted as gatekeepers to form dsDNA-functionalized MOFs. Additionally, Exo I was introduced into the system to accelerate the release of the signal molecules. In the presence of biological targets, the competitive binding between the targets and aptamers caused the hydrolysis of the free DNA sequence by Exo I, promoting the release of signal molecules and leading to a rapid and significant increase in the fluorescence intensity. For adenosine triphosphate (ATP) and cytochrome *c* (cyt *c*), which were chosen as model biological targets, this sensor displayed detection limits as low as 5.03 and 6.11 fM, respectively. Moreover, the developed biosensor was successfully applied to the simultaneous detection of ATP and cyt *c* in spiked serum samples. Therefore, this strategy provides guidance for further research of biosensors for simultaneous multiple-target detection and propels the application of MOF carriers in biomedicine.

1. Introduction

Simultaneous multiple-target detection is essential for the prevention, identification, and treatment of numerous diseases, because diagnostic processes are fundamental in the effective treatment of various diseases (Cheng et al., 2017; Shi et al., 2021). Hence, the exploitation of tools for simultaneous detection is critically important. To date, various nanomaterials, such as magnetic nanoparticles, quantum dots, and gold nanoparticles, have been used in biosensing structures for simultaneous multiple-target detection (He et al., 2019; Wang et al., 2020a,b; Wu et al., 2021). Considering the need to analyze an ever-increasing number of biological targets in complex mixtures, current studies have focused on the development of a general biosensor platform capable of measuring multiple biological targets in parallel.

Metal-organic frameworks (MOFs) have been extensively applied in the biomedical field, owing to their ultrahigh surface area, unique porosity, chemical tenability, and functional biodegradability (Bai et al., 2016; Cai et al., 2019; Riccò et al., 2018). At an early stage, molecular imaging probes and drug delivery carriers are the dominant applications of MOFs in biomedicine (Horcajada et al., 2010; Wang and Astruc, 2020). MOFs have chemical moieties, such as amino or azide groups, which allow the generation of novel biofunctional materials by the accurate grafting of biomolecules such as enzymes (Doherty et al., 2013), nucleotides (Morris et al., 2014), antibodies (Qi et al., 2017), and peptides (Bonnefoy et al., 2015). Hence, biofunctional MOFs have great potential to realize signal transduction and selective recognition

* Corresponding author. Key Laboratory of Marine Environmental Corrosion and Bio-fouling, Institute of Oceanology, Chinese Academy of Sciences, Qingdao, 266071, China.
** Corresponding author. Key Laboratory of Marine Environmental Corrosion and Bio-fouling, Institute of Oceanology, Chinese Academy of Sciences, Qingdao, 266071, China.
E-mail addresses: zhangdun@qdio.ac.cn (D. Zhang), qipeng@qdio.ac.cn (P. Qi).

https://doi.org/10.1016/j.bios.2021.113817
Received 14 August 2021; Received in revised form 4 November 2021; Accepted 15 November 2021
Available online 22 November 2021

(Doonan et al., 2017; Meng et al., 2020a,b; He et al., 2017), which can be used to establish biosensors for simultaneous multiple-target detection. UiO family comprises typical MOFs, of which UiO-66 is considered the prototype and most prominent member (Eddaoudi et al., 2002). UiO-66 possesses well-defined porosity and a very high surface area, allowing it to encapsulate a mass of signal molecules (Zhou et al., 2012). Moreover, signal molecules can be controlled and released in response to external chemical or physical stimuli. Based on these advantages, UiO-66 has been widely applied to target detection (Bai et al., 2019; Du et al., 2019; Gao et al., 2021; Guo et al., 2017; Huang et al., 2021; Meng et al., 2020a, b; Wang et al., 2020a,b; H. S. Wang et al., 2017b; Z. Wang et al., 2017a; Yan et al., 2018). However, as a supporting platform for encapsulating signal molecules, UiO-66 usually encounters the limitations of low load capacities and time-consuming responsive processes (Bao et al., 2020; Feng et al., 2021; Jarai et al., 2020; Jodłowski et al., 2021; Zhu et al., 2014), which lead to the adverse development of UiO applications.

To mitigate these limitations, we designed and developed a novel platform based on target-modulated competitive binding and exonuclease I (Exo I)-powered signal molecule release for simultaneous multiple-target detection. UiO-67 was chosen to replace UiO-66 as the supporting platform for encapsulating more signal molecules. Compared to UiO-66, which comprises terephthalic acid, UiO-67 employs diphenyl-4,4′-dicarboxylic acid as the organic ligand. Thus, UiO-67 possesses larger octahedral and tetrahedral holes with diameters of 23 and 11.5 Å, owing to the longer linkers (Katz et al., 2013). Moreover, Exo I with excellent hydrolysis efficiency was introduced into the system to accelerate the release of the signal molecules. Therefore, the proposed method decreases the time necessary to reach equilibrium and achieves a rapid response.

The preparation and detection processes of the system are illustrated in Fig. 1: 2-Amino-[1,1′-biphenyl]-4,4′-dicarboxylic acid was used as the organic ligand to synthesize the highly stable aminated UiO-67 (UiO-67-NH_2) by a one-step hydrothermal method. The amino group in UiO-67-NH_2 can be easily post-modified to obtain other characteristics, and thus, the single-stranded DNA (ssDNA) S_X (X = ATP or cyt *c*) with a carboxyl group can be linked to the UiO-67-NH_2 surface through an amide reaction. Subsequently, the fluorescent dyes were encapsulated in the multiple mesopores of the MOF by the aptamer ssDNA A_X (X = ATP or cyt *c*), which was partially hybridized with S_X, and the assembled double-stranded DNA (dsDNA) structure acted as a gatekeeper to form dsDNA-functionalized MOFs. According to this method, two dsDNA-functionalized MOFs loaded with different dyes, Rho 6G@UiO-67 and Cy5@UiO-67, were synthesized for the simultaneous detection of ATP and cyt *c*. Notably, the dsDNA structure effectively prevented the hydrolysis of Exo I, which is a monomeric enzyme that catalyzes the hydrolysis of ssDNA in the 3′–5′ direction to form mononucleotides, but not dsDNA (Breyer and Matthews, 2000; Gao et al., 2020; Wu et al., 2009). In the absence of biological targets, capping duplex structures hindered the release of signal molecules. On the other hand, in the presence of targets, the aptamer ssDNA A_X combined with the targets to form target–aptamer complexes away from the MOFs, thereby unlocking the caps of MOFs and releasing the signal molecules. Furthermore, the free S_X of the MOFs were degraded from the 3′-end by Exo I, thereby reducing the steric hindrance and promoting the release of the signal molecules. This platform was developed as a versatile biosensing method for the simultaneous detection of biological targets with the advantages of rapid response, high sensitivity, and selectivity; and propels the application of MOF carriers in biomedicine.

2. Experimental section

2.1. Chemicals and materials

All DNA sequences were ordered from Sangon Biotechnology Co., Ltd. (Shanghai, China) and were listed in Table S1. Exo I (extracted from *E. coli*, 20 U μL^{-1}) was obtained from Thermo Fisher Scientific (Waltham, MA, USA), while human serum samples were obtained from Solarbio Co., Ltd. (Beijing, China). $ZrCl_4$, 2-aminoterephthalic acid (BDC-NH_2), and 2-amino-[1,1′-biphenyl]-4,4′-dicarboxylic acid (H_2BPDC-NH_2) were purchased from Aladdin Reagent Co., Ltd. (Shanghai, China). Rhodamine 6G (Rho 6G), cyanine 5 carboxylic acid (Cy5), ATP, CTP, AMP, ADP, cyt *c*, dopamine, urea, glucose, glutathione (GSH), and L-cysteine were purchased from Sigma-Aldrich Co., Ltd. (Beijing, China). All chemicals used in this assay were of analytical grade and were used without further purification. Ultrapure water was used for all the experiments.

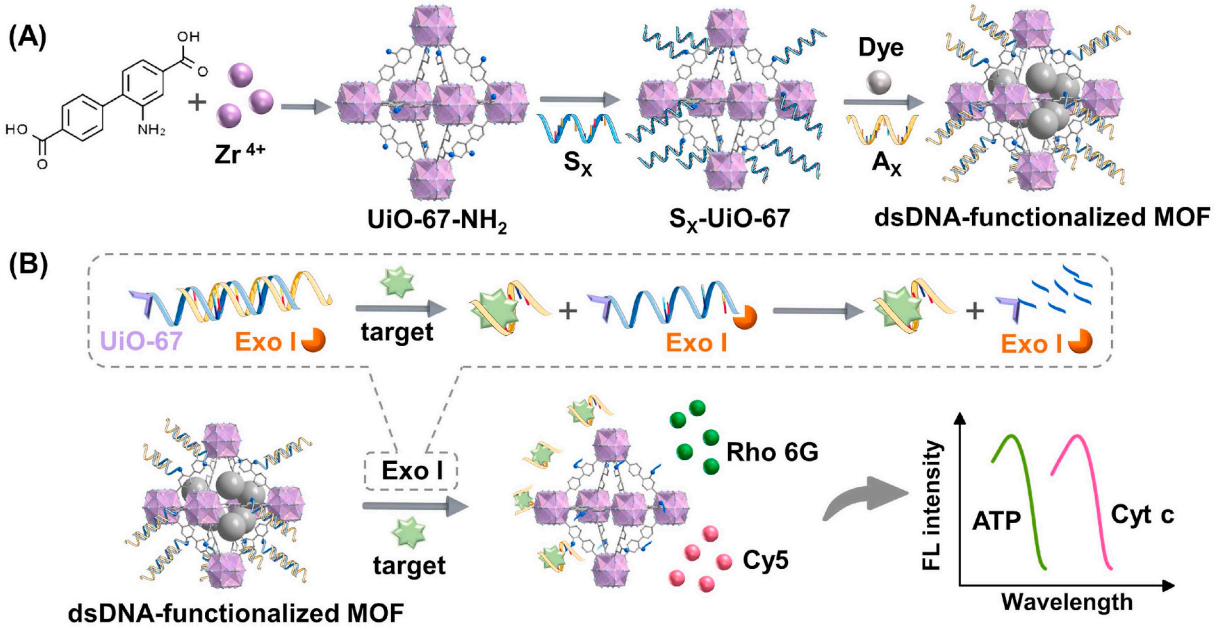

Fig. 1. Schematic illustration of the preparation of dsDNA-functionalized MOF (A) and target-modulated competitive binding and Exonuclease I-powered strategy for simultaneous and rapid detection of biological targets (B).

2.2. Synthesis of UiO-66-NH_2 and UiO-67-NH_2

The MOFs were prepared according to a previously reported procedure with slight modification (Jasuja et al., 2015; Wu et al., 2018). Briefly, 488 mg $ZrCl_4$ and 188 mg BDC-NH_2 were dissolved in 30 mL DMF via ultrasonication for 15 min. Next, 3.6 mL acetic acid was added to the solution and ultrasonicated for 5 min. Subsequently, the mixture was allowed to react for 24 h at 100 °C under static conditions to yield UiO-66-NH_2. To synthesize UiO-67-NH_2, BDC-NH_2 was replaced with 267 mg H_2BPDC-NH_2 and reacted under the same reaction conditions. The resulting MOF products were centrifuged (10000 r min^{-1}, 5 min) and washed with DMF and absolute ethanol for 3 times respectively. Finally, the MOFs were vacuum-dried at 50 °C for 5 h.

2.3. Synthesis of dsDNA-functionalized MOFs

Two dsDNA-functionalized MOFs loaded with different dyes, Rho 6G@UiO-67 and Cy5@UiO-67, were synthesized for the simultaneous detection of ATP and cyt *c*. To fabricate Rho 6G@UiO-67, 250 μL $S_{Rho\ 6G}$ (100 μM) was mixed with 125 μL EDC (5 mg mL^{-1}) and 125 μL NHS (5 mg mL^{-1}) for 20 min. Next, 5 mg UiO-67-NH_2 was added to the reaction mixture and stirred for 15 h. Subsequently, the obtained $S_{Rho\ 6G}$-UiO-67 was washed with PBS (10 mM, pH = 7.4) for 3 times and dispersed into 500 μL PBS solution. To load the Rho 6G, 100 μL $S_{Rho\ 6G}$-UiO-67 solution was incubated with 80 μL Rho 6G (1 mM) for 12 h under stirring. Subsequently, 20 μL $A_{Rho\ 6G}$ (10 μM) solution was added to the mixture and reacted for 3 h to form the dsDNA-functionalized MOFs, Rho 6G@UiO-67. The prepared products were washed with PBS and redispersed in 100 μL PBS. The other dsDNA-functionalized MOFs were prepared using a similar method.

2.4. Feasibility of the novel platform based on UiO-67 and Exo I

To investigate the feasibility of the novel platform based on UiO-67 and Exo I, the dye release profiles of Rho 6G@UiO-66 and Rho 6G@UiO-67 were determined. Thus, 40 μL Rho 6G@UiO-66 (250 μg mL^{-1}) was first added to 300 μL PBS (10 mM, pH = 7.4), 20 μL Exo I (800 U mL^{-1}) and 40 μL ATP solution (10 nM) were then added to the sample. Then, 100 μL aliquots of the solution were centrifuged for 3 min at 10000 rpm, and the fluorescence spectra of Rho 6G@UiO-67 were recorded. The fluorescence was excited at 525 nm and recorded in the range 540–700 nm. The release profile of the dye from Rho 6G@UiO-67 was attained using the same method.

2.5. Simultaneous detection of ATP and cyt c

To detect ATP and cyt *c* simultaneously, 40 μL Rho 6G@UiO-67 (250 μg mL^{-1}), 40 μL Cy5@UiO-67 (250 μg mL^{-1}), and 20 μL Exo I (800 U mL^{-1}) were mixed in 260 μL PBS solution. Then, 40 μL biological target sample containing ATP and cyt *c* at specified concentrations was added to the mixture and incubated for 15 min. The fluorescence spectrum of each supernatant was then recorded. For Rho 6G, the fluorescence was excited at 525 nm and recorded in the range of 540–700 nm, while for Cy5, the fluorescence was excited at 646 nm and recorded in the range of 650–800 nm.

2.6. Real sample assay

For real sample detection, human serum samples were used for the spike-and-recovery study. The various concentrations of ATP and cyt *c* standards were dissolved in 10% human serum diluted with PBS buffer (10 mM, pH=7.4), and the concentrations of ATP and cyt *c* in the resultant solutions were determined from the fluorescence responses.

3. Results and discussion

3.1. Characterization of MOFs

UiO-67-NH_2 was obtained from $ZrCl_4$ and H_2BPDC-NH_2 through a facile one-pot hydrothermal method. Transmission electron microscopy (TEM) was employed to characterize the morphologies of the prepared UiO-67-NH_2 nanoparticles. As shown in Fig. 2A, UiO-67-NH_2 was a homogeneous nanoparticle with a rough surface, uniform size, and an average diameter of 110–150 nm. Further, Fig. 2B shows the X-ray diffraction (XRD) pattern of UiO-67-NH_2, which completely matched the simulated pattern of pure phase UiO-67-NH_2 (Liu et al., 2021a), revealing its purity and high crystallinity.

Subsequently, the UiO-67-NH_2 nanoparticles were modified to form dsDNA-functionalized MOFs. To confirm the formation of the dsDNA-functionalized MOFs, TEM analysis and Fourier transform infrared spectroscopy (FTIR) were next conducted. As shown in Fig. 2C, the sizes of the Rho 6G@UiO-67 composites were similar to that of bare UiO-67-NH_2, indicating that the load of Rho 6G had little effect on the morphology of UiO-67-NH_2. Furthermore, the FTIR spectra of UiO-67-NH_2, S_X-UiO-67, and Rho 6G@UiO-67 were recorded to verify the effective encapsulation of the dyes (Fig. 2D). Notably, the vibrational transitions of UiO-67-NH_2 have been previously discussed in the literature (Binaeian et al., 2021; Yang et al., 2020). A cluster of peaks in the range 1400–1680 cm^{-1} was assigned to the asymmetric and symmetric stretching modes of the carboxylate group (1409 and 1597 cm^{-1}) and ring stretching mode (1541 cm^{-1}) of the organic linker. The distinct peaks at 660 and 771 cm^{-1} were assigned to Zr–O in the longitudinal and transverse modes, which are characteristic to the bonds of UiO-67-NH_2. Additionally, the appearance of new peaks at 1016 cm^{-1} (C–N) in the S_X-UiO-67 and Rho 6G@UiO-67 spectra, compared to that of UIO-66-NH_2, were assigned to the DNA chains. This indicated the formation of an amide bond between UiO-67-NH_2 amino group and S_X carboxyl group, and the assembly of the dsDNA structure to form gatekeepers of dsDNA-functionalized MOFs.

3.2. Feasibility of the novel platform based on UiO-67 and Exo I

In this work, a new platform based on UiO-67 and Exo I was established to increase the encapsulated capacity of MOF carriers and accelerate the release process of signal molecules. To confirm the feasibility of this method, the fluorescence responses of the released dyes from Rho 6G@UiO-67 under different conditions were recorded. As illustrated in Fig. 3A, an increased fluorescence signal was observed in the sample following the addition of ATP, indicating the excellent response of Rho 6G@UiO-67 toward ATP targets. Moreover, the fluorescence signal was significantly increased after Exo I was added to hydrolyze the free dsDNA S_X, proving that the addition of Exo I accelerated the release of the signal molecules. These results confirmed that the developed target-modulated competitive binding and Exo I-powered strategy shows great potential as a method to construct biosensors.

In this strategy, UiO-67 was chosen to replace UiO-66, a typical MOF, as the carrier to load more signal molecules. As displayed in Fig. 3B, UiO-66 employed terephthalic acid as the organic ligand, while UiO-67 replaced the organic ligand with diphenyl-4,4′-dicarboxylic acid. The stability of the UiO structures was not reduced by the extension of the linkers to two benzene rings. In contrast, the micropore volume increased from 0.43 to 0.85 $cm^3\ g^{-1}$, while the Langmuir surface area increased from 1281 to 2483 $m^2\ g^{-1}$ (Katz et al., 2013; Peterson et al., 2015). Consequently, UiO-67, with longer linkers, possessed larger octahedral and tetrahedral holes to store more signal molecules. To compare the encapsulated capabilities of UiO-66 and UiO-67, Rho 6G molecules were separately loaded in UiO-66 and UiO-67 and assembled into Rho 6G@UiO-66 and Rho 6G@UiO-67, respectively. The fluorescence intensities of the released dyes from Rho 6G@UiO-66 and Rho 6G@UiO-67 at different times were illustrated in Fig. 3C. The curves

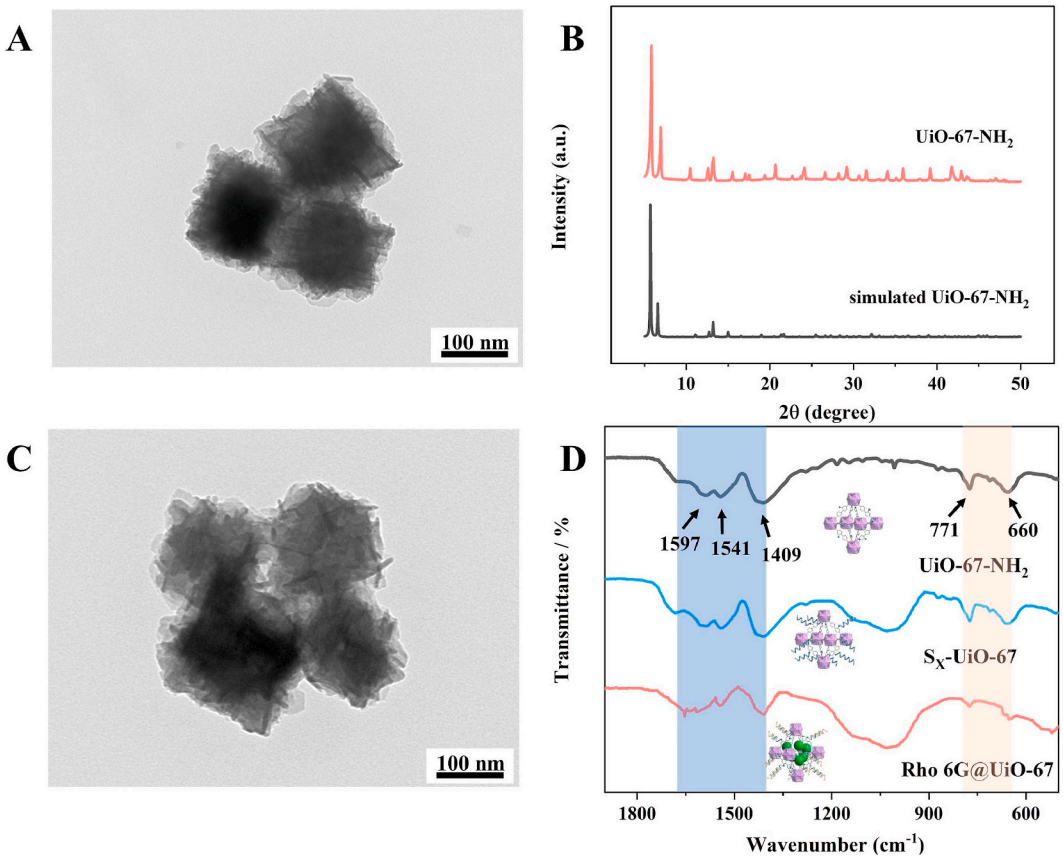

Fig. 2. TEM images of the prepared UiO-67-NH_2 (A) and Rho 6G@UiO-67 (C). XRD patterns of experimental and simulated UiO-67-NH_2 (B). FTIR spectra of the UiO-67-NH_2, S_X-UiO-67, and Rho 6G@UiO-67 (D).

shown very small changes in the sample without added ATP in 30 min, indicating that the capping duplex structures consisting of A_X and S_X hindered the release of the dyes. Once the targets appeared, a progressively increasing fluorescence signal was obtained, which was attributed to the caps of MOFs unlocking through a competitive displacement reaction. However, in the absence of Exo I, the fluorescence response of Rho 6G@UiO-66 and Rho 6G@UiO-67 barely reached equilibrium in 30 min. After the addition of Exo I, the fluorescence intensities increased significantly and began to level off after 15 min, demonstrating that the addition of Exo I significantly accelerated the release of the dyes from the MOFs. This phenomenon was attributed to the free dsDNA S_X being hydrolyzed by Exo I, resulting in a decrease in steric hindrance. Notably, the addition of Exo I effectively overcame the time-consuming limitation of UiO-66 and UiO-67 in molecules releasing, which usually took hours to acquire the equilibrium (Table S2).

To quantify the effect of Exo I, which directly accelerates dyes release, the release increments were calculated according to the fluorescence intensity at 552 nm using the following formula:

$$\text{Release increment (a.u.)} = \text{FL intensity}_{\text{ATP and Exo I}} - \text{FL intensity}_{\text{ATP}}$$

where $FL\ intensity_{ATP\ and\ Exo\ I}$ and $FL\ intensity_{ATP}$ are the fluorescence intensity of the reaction solution in the presence and absence of Exo I, respectively. As shown in Fig. 3D, the fluorescence intensities increased significantly after treatment with Exo I for only 1 min, indicating the high efficiency of Exo I in promoting the release of the signal molecules. More importantly, the *release increment* of Rho 6G@UiO-67 was significantly higher than that of Rho 6G@UiO-66 at the same testing time. This was attributed to the larger octahedral and tetrahedral holes of Rho 6G@UiO-67, which allowed more dyes to be stored, and thus, more dyes were released after Exo I treatment.

In addition, the morphologies of the dsDNA-functionalized MOFs before and after treated with ATP and Exo I were characterized by TEM (Fig. 3E–H). The results revealed that the diameters of the dsDNA-functionalized MOF composites were similar to that of the sample treated with ATP and Exo I. This indicated that the release of Rho 6G and the hydrolysis of the dsDNA structure immobilized onto the MOF surfaces had little effect on the morphologies of the dsDNA-functionalized MOFs. Overall, the feasibility of the novel platform based on UiO-67 and Exo I to increase the encapsulated capacity of the MOF carrier and accelerate the responsive process was verified.

3.3. Assay performance

To achieve the ideal performances for detecting biological targets, the concentration of Exo I, reaction time, and dsDNA-functionalized MOF concentration were optimized. Exo I was used to accelerate the dyes release from the dsDNA-functionalized MOFs, and the amount of Exo I greatly affected the performance of the developed system. As demonstrated in Fig. S1A, the Exo I concentration-dependent fluorescence intensity increased until it peaked at 40 U mL^{-1}, indicating that 40 U mL^{-1} Exo I ensured the rapid catalytic equilibrium of the Rho 6G@UiO-67 system for the detection of ATP. The fluorescence intensities exhibited similar trends in the Cy5@UiO-67 system (Fig. S1B). Hence, 40 U mL^{-1} was chosen as the optimal Exo I concentration. Furthermore, Fig. S1C and Fig. S1D revealed that the fluorescence responses climbed up with increasing reaction time from 1 to 15 min, after which only slightly improved responses were observed. Therefore, 15 min was deemed sufficient to release the dyes, which also demonstrated the high efficiency of Exo I for promoting the release of the signal molecules. Moreover, the effects of the dsDNA-functionalized MOF concentrations were also studied. Fig. S1E clearly shows that the fluorescence intensity gradually increased with increasing Rho 6G@UiO-67 concentration from 10 to 25 μg mL^{-1}, and stabilized when the

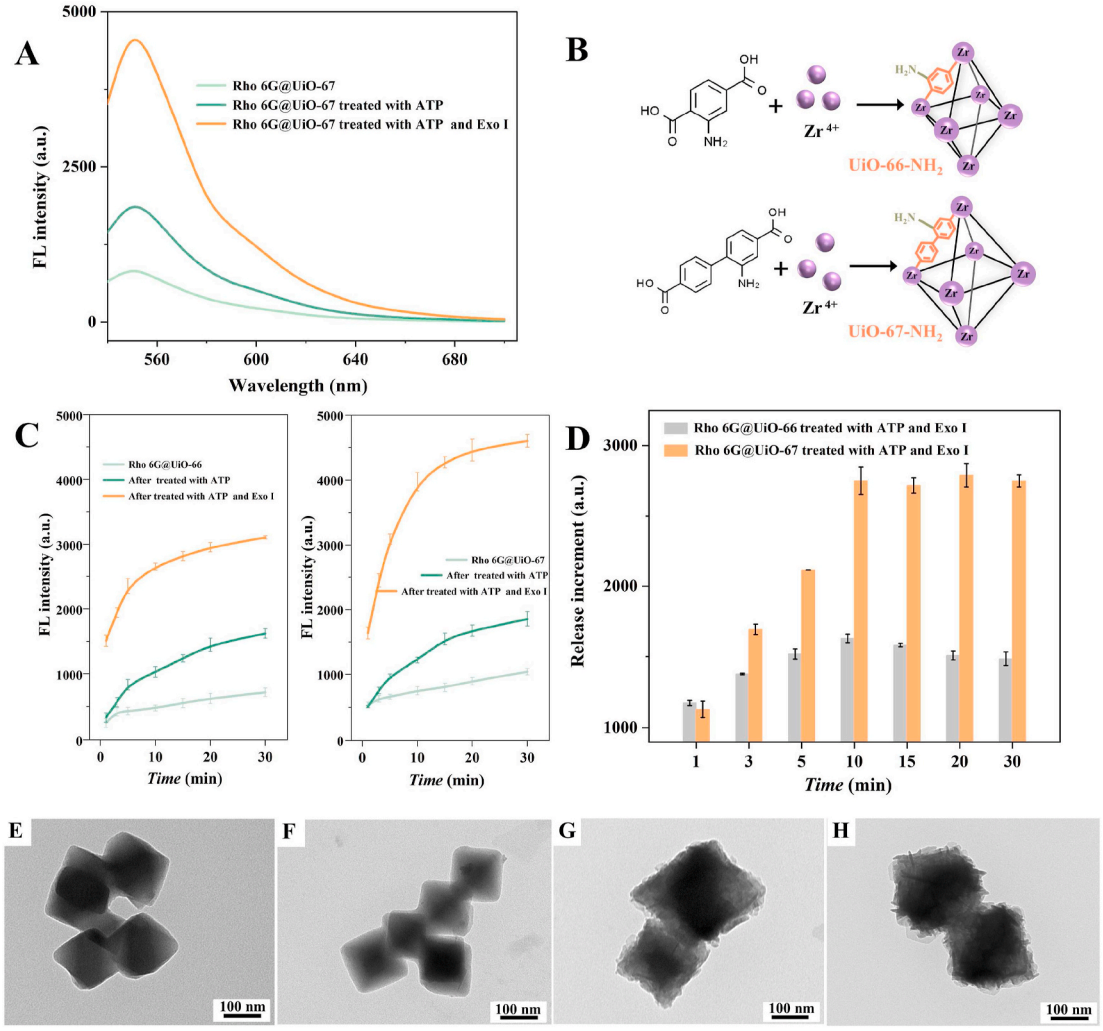

Fig. 3. Fluorescence spectra of the released dyes from Rho 6G@UiO-67 before and after treated with 1 nM ATP or 1 nM ATP and 40 U mL^{-1} Exo I for 15 min (A). Schematic diagram of UiO-66-NH_2 and UiO-67-NH_2 synthesis (B). Fluorescence intensities of released dyes from Rho 6G@UiO-66 (left) and Rho 6G@UiO-67 (right) before and after treated with 1 nM ATP or 1 nM ATP and 40 U mL^{-1} Exo I (C). The *release increment* of dyes from Rho 6G@UiO-66 and Rho 6G@UiO-67 after treated with 1 nM ATP and 40 U mL^{-1} Exo I (D). TEM images of the prepared Rho 6G@UiO-66 and Rho 6G@UiO-67 before (E, G) and after treated with 1 nM ATP and 40 U mL^{-1} Exo I for 15 min (F, H). Error bars represent standard deviation, n=5.

concentration exceeded 25 μg mL^{-1}. The optimization of the Cy5@UiO-67 concentration showed similar trends in cyt *c* detection (Fig. S1F). Hence, 25 μg mL^{-1} dsDNA-functionalized MOF was chosen for the subsequent experiments.

Using the established optimal experimental conditions, we next evaluated the sensitivity and selectivity of the proposed biosensor versus the targets. The results of the fluorescence experiments for the two biological analytes were shown in Fig. 4. For the ATP samples, the fluorescence intensity increased with enhancing ATP concentration (Fig. 4A). As shown in Fig. 4B, the fluorescence intensity at the maximum emission wavelength exhibited good linear dependence on the logarithm of the ATP concentration in the range 8–1000 fM. The linear regression equation was *FL intensity* = 1316.32 log C_{ATP} + 433.6 and the correlation coefficient (R^2) was 0.994. The limit of detection (LOD) for ATP was calculated to be 5.03 fM (S/N = 3). In addition, to evaluate the selectivity of the proposed method, ADP, AMP, and CTP were chosen as the model interfering substances, with concentrations of ATP and the interfering substances of 1 nM. As shown in Fig. 4C, the fluorescence responses of the interfering substances were similar to those of the blank sample. However, the addition of ATP caused a significant fluorescent response, indicating that only ATP could be recognized by the aptamer to trigger the following Exo I-powered dyes release.

The fluorescence response of Cy5@UiO-67 versus different cyt *c* concentrations in the range 10–1000 fM was next investigated. Fig. 4D showed that the fluorescence intensity increased with increasing cyt *c* concentration. The fluorescent intensity and logarithm of cyt *c* concentration possessed a good linear relationship (Fig. 4E), with the linear regression equation *FL intensity* = 1144.74 log $C_{cyt\ c}$ + 284.09 (R^2 = *0.992*). The LOD for cyt *c* was calculated to be 6.11 fM (S/N = 3). Moreover, selectivity tests were performed with dopamine, urea, glucose, GSH, and L-cysteine, and the concentration of each sample was 1 nM. As depicted in Fig. 4F, the addition of interfering substances afforded a negligible response, indicating the high selectivity of Cy5@UiO-67 toward the cyt *c* targets.

These results demonstrate that the proposed biosensor can be used for the quantitative analysis of biological targets. Compared to other studies of ATP and cyt *c* detection (Table S3), the suggested method performed at lower limits. This high sensitivity may be related to the highly porous structure, which permits the encapsulation of abundant dyes, and the excellent hydrolysis effect of Exo I, which allows the release of numerous dyes in the presence of just a few biological targets. Moreover, as gatekeepers of dsDNA-functionalized MOFs, the aptamer chains ensured high selectivity for detection. Overall, the developed

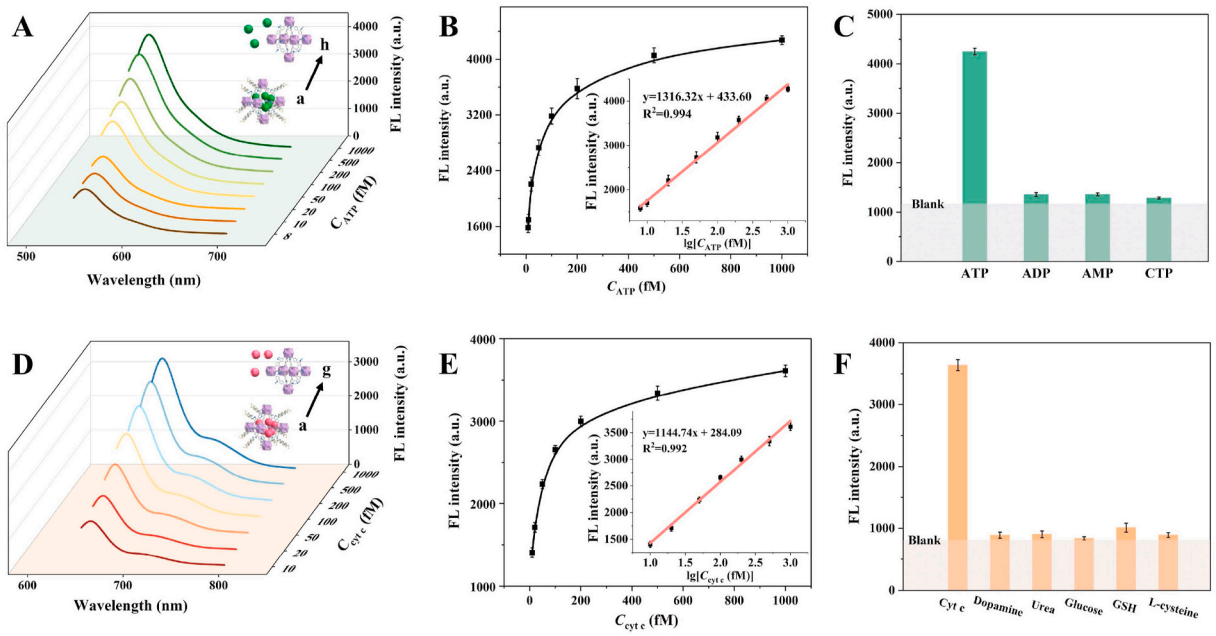

Fig. 4. Fluorescence intensities of the proposed biosensor obtained from different ATP concentrations: (a–h) 8, 10, 20, 50, 100, 200, 500, and 1000 fM (A). Fluorescence intensity at maximum emission wavelength versus ATP concentration in the range of 8–1000 fM; inset shows the linear relationship between the change of fluorescence intensity and logarithm of ATP concentration (B). Selectivity of the biosensor with different interferences (C). Fluorescence intensities of the proposed biosensor obtained from different cyt *c* concentrations: (a–g) 10, 20, 50, 100, 200, 500, and 1000 fM (D). Fluorescence intensity at maximum emission wavelength versus cyt *c* concentration in the range of 10–1000 fM; inset shows the linear relationship between the change of fluorescence intensity and logarithm of cyt *c* concentration (E). Selectivity of the biosensor with different interferences (F). Error bars represent standard deviation, n=5.

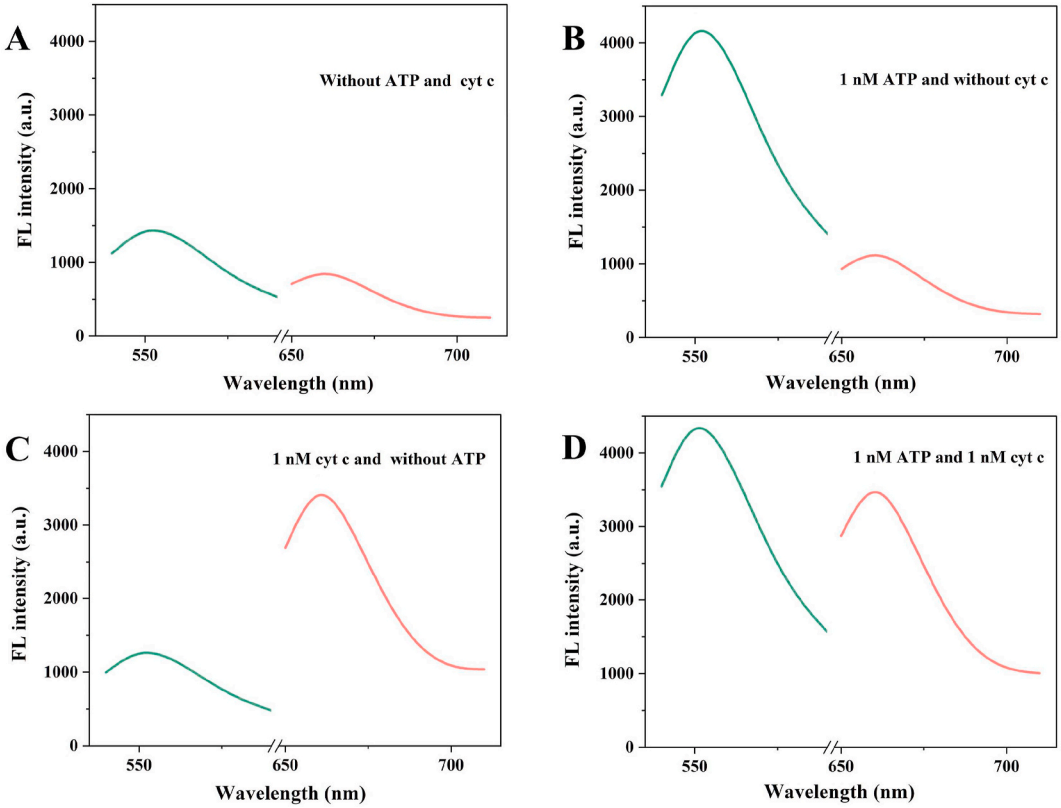

Fig. 5. The fluorescence spectra of released dyes from Rho 6G@UiO-67 and Cy5@UiO-67 after treated with no targets (A), 1 nM ATP (B), 1 nM cyt *c* (C), and 1 nM ATP and 1 nM cyt *c* (D).

biosensor based on UiO-67 and Exo I possessed the advantages of a rapid response, simple operation, and easy fabrication, and shows great potential as a powerful tool for detecting biological targets with high sensitivity and selectivity.

3.4. Simultaneous detection performances of dual biological targets

The simultaneous detection of multiple biological targets is vital for molecular diagnosis. Given the excellent ability of the dsDNA-functionalized MOFs to analyze a single biological target, multiple-target detection can be realized by using the developed biosensor. To verify the ability for simultaneous detection of biological targets, ATP and cyt *c* were chosen as model targets. The fluorescence responses of Rho 6G@UiO-67 and Cy5@UiO-67 towards ATP and cyt *c* under different conditions were recorded, and the results were shown in Fig. 5A–D. Without the targets, the fluorescence intensities at the maximum emission wavelengths of the released dyes from Rho 6G@UiO-67 and Cy5@UiO-67 were only 1365 and 849 a.u., respectively. On the other hand, in the sole presence of ATP, the fluorescence intensity of the released dyes from Rho 6G@UiO-67 increased to 4161 a.u., whereas that of Cy5@UiO-67 only changed slightly. In contrast, in the sole presence of cyt *c*, the fluorescence intensity of the released dyes from Cy5@UiO-67 increased to 3418 a.u., while that of Rho 6G@UiO-67 only changed slightly. More importantly, when in the presence of both ATP and cyt *c*, the fluorescence intensities of the released dyes from Rho 6G@UiO-67 and Cy5@UiO-67 increased to 4300 and 3473 a.u., respectively. The significant differences in the fluorescence response revealed the ability of the developed method for multicolor and highly selective detection of biological targets. Indeed, the developed system meets the demands of simultaneous multiple-target detection through fluorescence response variation and provides a rapid and versatile platform for molecular diagnostics.

3.5. Real sample assay

To evaluate the practical application capability of the proposed biosensor in real samples, various concentrations of ATP and cyt *c* were spiked in diluted 10% human serum samples for the recovery experiments. As shown in Table S4, the recovery rates for ATP were distributed between 96.7 and 103.1% with a relative standard deviation (RSD) ranging from 1.4 to 4.7%. The recovery rates for cyt *c* were in the range of 97.3–107.1% with an acceptable RSD of 2.4–4.8%. The analytical results indicated the satisfactory practicability of the developed sensor for the simultaneous detection of biological targets in real samples.

4. Conclusion

A diagnostic method for the rapid and simultaneous detection of dual biological targets in a single assay was demonstrated in this study. The method design was based on target competitive binding with the DNA aptamer and Exo I-powered signal molecule release. The analytical parameters of the experiment, namely the Exo I concentration, reaction time, and dsDNA-functionalized MOF concentration, were evaluated for optimal detection conditions. Subsequently, ATP and cyt *c* were quantitatively detected within 15 min in one simple step, and the detection limits of ATP and cyt *c* were reduced to 5.03 and 6.11 fM, respectively. Furthermore, the developed biosensor was successfully applied to the simultaneous detection of ATP and cyt *c* in spiked serum samples with high accuracy. However, the complex synthesis of dsDNA-functionalized UiO-67 may limit its further application, and thus simpler fabrication processes need to be further explored. Notably, compared to previously reported biosensors based on Zr-MOFs, the proposed method has the following merits: Firstly, the selected nanocarrier UiO-67 possessed larger octahedral and tetrahedral holes for encapsulating signal molecules than typical Zr-MOFs (UiO-66), thus improving the detection sensitivity of the biosensor. Secondly, with the assistance of Exo I-promoted signal molecule release, the detection response time was significantly reduced, and the sensitivity was further improved. Thirdly and most importantly, the rapid and simultaneous detection of other biological targets can be achieved by simply changing the dyes and capping dsDNA structures. Therefore, this strategy possesses the advantages of rapid response, high sensitivity, and selectivity; provides a versatile platform for simultaneous multiple-target detection; and propels the application of MOF carriers in biomedicine.

CRediT authorship contribution statement

Yingwen Wang: Conceptualization, Methodology, Formal analysis, Investigation, Writing – original draft. **Dun Zhang:** Writing – review & editing, Supervision. **Yan Zeng:** Writing – review & editing. **Peng Qi:** Investigation, Writing – review & editing, Supervision, Funding acquisition.

Declaration of competing interest

The authors declare that they have no known competing financial interests or personal relationships that could have appeared to influence the work reported in this paper.

Acknowledgements

This work was supported by the National Natural Science Foundation of China (Grant Nos. 41876101 and 41906037) and Nantong Scientific Plan Foundation (Grant Nos. JC2021054 and 2020NT04).

Appendix A. Supplementary data

Supplementary data to this article can be found online at https://doi.org/10.1016/j.bios.2021.113817.

References

Bai, J., Liu, L., Jia, C., Liu, Z., Gao, S., Han, Y., Yan, H., 2019. ACS Appl. Bio Mater. 2 (12), 6021–6028.
Bai, Y., Dou, Y., Xie, L.H., Rutledge, W., Li, J.R., Zhou, H.C., 2016. Chem. Soc. Rev. 45 (8), 2327–2367.
Bao, T., Fu, R., Wen, W., Zhang, X., Wang, S., 2020. ACS Appl. Mater. Interfaces 12 (21), 2087–2094.
Binaeian, E., Li, Y., Tayebi, H.A., Yuan, D., 2021. J. Hazard Mater. 416, 125933.
Bonnefoy, J., Legrand, A., Quadrelli, E.A., Canivet, J., Farrusseng, D., 2015. J. Am. Chem. Soc. 137 (29), 9409–9416.
Breyer, W.A., Matthews, B.W., 2000. Nat. Struct. Biol. 7 (12), 1125–1128.
Cai, H., Huang, Y.L., Coordin, D.L., 2019. Chem. Rev. 378, 207–221.
Cheng, Z., Choi, N., Wang, R., Lee, S., Moon, K.C., Yoon, S.Y., Chen, L., 2017. J. Choo ACS Nano 11 (5), 4926–4933.
Doherty, C.M., Grenci, G., Ricco, R., Mardel, J.I., Reboul, J., Furukawa, S., Kitagawa, S., Hill, A.J., Falcaro, P., 2013. Adv. Mater. 25 (34), 4701–4705.
Doonan, C., Ricco, R., Liang, K., Bradshaw, D., Falcaro, P., 2017. Acc. Chem. Res. 50 (6), 1423–1432.
Du, L., Chen, W., Wang, J., Cai, W., Kong, S., Wu, C., 2019. Sensor. Actuator. B Chem. 301, 127073.
Eddaoudi, M., Kim, J., Rosi, N., Vodak, D., Wachter, J., O'Keeffe, M., Yaghi, O.M., 2002. Science 295 (5554), 469–472.
Feng, J., Chu, C., Dang, K., Yao, T., Ma, Z., Han, H., 2021. Anal. Chim. Acta 1187, 339170.
Gao, X., Qi, L., Liu, K., Meng, C., Li, Y., Yu, H.Z., 2020. Anal. Chem. 92 (9), 6229–6234.
Gao, X., Sun, G., Wang, X., Lin, X., Wang, S., Liu, Y., 2021. Sensor. Actuator. B Chem. 331, 129448.
Guo, C., Su, F., Song, Y., Hu, B., Wang, M., He, L., Peng, D., Zhang, Z., 2017. ACS Appl. Mater. Interfaces 9 (47), 41188–41199.
He, J., Li, G., Hu, Y., 2017. Mikrochim. Acta 184, 2365–2373.
He, Y., Chen, S., Huang, L., Wang, Z., Wu, Y., Fu, F., 2019. Anal. Chem. 91 (1), 1171–1177.
Horcajada, P., Chalati, T., Serre, C., Gillet, B., Sebrie, C., Baati, T., Eubank, J.F., Heurtaux, D., Clayette, P., Kreuz, C., Chang, J.S., Hwang, Y.K., Marsaud, V., Bories, P.N., Cynober, L., Gil, S., Ferey, G., Couvreur, P., Gref, R., 2010. Nat. Mater. 9 (2), 172–178.
Huang, W., Hu, G., Liang, W., Wang, J., Lu, M., Yuan, R., Xiao, D., 2021. Anal. Chem. 93 (15), 6239–6245.
Jarai, B.M., Stillman, Z., Attia, L., Decker, G.E., Bloch, E.D., Fromen, C.A., 2020. ACS Appl. Mater. Interfaces 12 (35), 38989–39400.

Jasuja, H., Peterson, G.W., Decoste, J.B., Browe, M.A., Walton, K.S., 2015. Chem. Eng. Sci. 124, 118–124.
Meng, T., Shang, N., Nsabimana, A., Ye, H., Wang, H., Wang, C., Zhang, Y., 2020a. Anal. Chim. Acta 1138, 59–68.
Jodłowski, P.J., Kurowski, G., Kuterasinski, Ł., Sitarz, M., Jelen, P., Jaskowska, J., Kołodziej, A., Pajdak, A., Majka, Z., Boguszewska-Czubara, A., 2021. ACS Appl. Mater. Interfaces 13 (1), 312–323.
Katz, M.J., Brown, Z.J., Colon, Y.J., Siu, P.W., Scheidt, K.A., Snurr, R.Q., Hupp, J.T., Farha, O.K., 2013. Chem. Commun. 49 (82), 9449–9451.
Meng, X.Z., Gu, H.W., Yi, H.C., He, Y.Q., Chen, Y., Sun, W.Y., 2020b. Anal. Chim. Acta 1125, 1–7.
Morris, W., Briley, W.E., Auyeung, E., Cabezas, M.D., Mirkin, C.A., 2014. J. Am. Chem. Soc. 136 (20), 7261–7264.
Peterson, G.W., Moon, S.Y., Wagner, G.W., Hall, M.G., DeCoste, J.B., Hupp, J.T., Farha, O.K., 2015. Inorg. Chem. 54 (20), 9684–9686.
Qi, X., Chang, Z., Zhang, D., Binder, K.J., Shen, S., Huang, Y.Y.S., Bai, Y., Wheatley, A.E. H., Liu, H., 2017. Chem. Mater. 29 (19), 8052–8056.
Riccò, R., Linder-Patton, O., Sumida, K., Styles, M.J., Liang, K., Amenitsch, H., Doonan, C.J., Falcaro, P., 2018. Chem. Mater. 30 (16), 5630–5638.
Shi, L., Liu, W., Li, B., Yang, C.J., Jin, Y., 2021. ACS Appl. Mater. Interfaces 13 (13), 15008–15016.
Wang, C., Liu, L., Liu, X., Chen, Y., Wang, X., Fan, D., Kuang, X., Sun, X., Wei, Q., Ju, H., 2020a. Sensor. Actuator. B Chem. 307, 127619.
Wang, J.J., Zheng, C., Jiang, Y.Z., Zheng, Z., Lin, M., Lin, Y., Zhang, Z.L., Wang, H., Pang, D.W., 2020b. Anal. Chem. 92 (1), 830–837.
Wang, Q., Astruc, D., 2020. Chem. Rev. 120 (2), 1438–1511.
Wang, Z., Yan, Z., Wang, F., Cai, J., Guo, L., Su, J., Liu, Y., 2017a. Biosens. Bioelectron. 97, 107–114.
Wang, H.S., Liu, H.L., Wang, K., Ding, Y., Xu, J.J., Xia, X.H., Chen, H.Y., 2017b. Anal. Chem. 89 (21), 11366–11371.
Wu, J., Zhou, X., Li, P., Lin, X., Wang, J., Hu, Z., Zhang, P., Chen, D., Cai, H., Niessner, R., Haisch, C., Sun, P., Zheng, Y., Jiang, Z., Zhou, H., 2021. Anal. Chem. 93 (25), 8799–8809.
Wu, Z., Zhen, Z., Jiang, J.H., Shen, G.L., Yu, R.Q., 2009. J. Am. Chem. Soc. 131 (34), 12325–12332.
Yan, Z., Wang, F., Deng, P., Wang, Y., Cai, K., Chen, Y., Wang, Z., Liu, Y., 2018. Biosens. Bioelectron. 109, 132–138.
Yang, Q., Hong, H., Luo, Y., 2020. Chem. Eng. J. 392, 123680.
Zhou, H.C., Long, J.R., Yaghi, O.M., 2012. Chem. Rev. 112 (2), 673–674.
Zhu, X., Gu, J., Wang, Y., Li, B., Li, Y., Zhao, W., Shi, J., 2014. Chem. Commun. 50, 8779–8782.